Inorganic Chemistry Communications 98 (2018) 34–40

Contents lists available at ScienceDirect

Inorganic Chemistry Communications

journal homepage: www.elsevier.com/locate/inoche

Short communication

Electronic structure, growth mechanism, and sonophotocatalytic properties of sphere-like self-assembled $NiWO_4$ nanocrystals

F.J.O. Rosal[a], A.F. Gouveia[a], J.C. Sczancoski[b], P.S. Lemos[b], E. Longo[c], B. Zhang[d], L.S. Cavalcante[a,*]

[a] PPGQ-CCN-DQ, Universidade Estadual do Piauí, Rua João Cabral, N. 2231, P.O. Box 381, 64002-150 Teresina, PI, Brazil
[b] CDMF, Universidade Federal de São Carlos, P.O. Box 676, 13565-905 São Carlos, SP, Brazil
[c] CDMF, Universidade Estadual Paulista, P.O. Box 355, 14801-907 Araraquara, SP, Brazil
[d] Department of Chemistry, Stony Brook University, Stony Brook, NY, USA

GRAPHICAL ABSTRACT

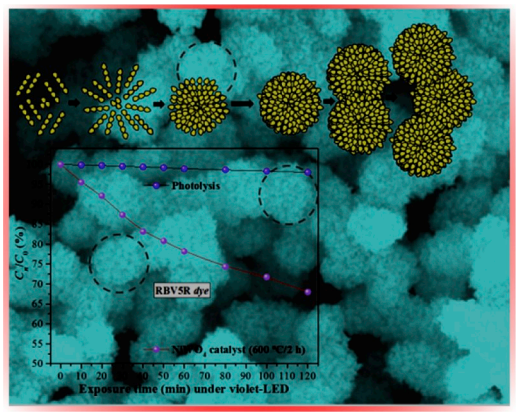

ARTICLE INFO

Keywords:
$NiWO_4$ nanocrystals
Growth mechanism
Optical band gap
Band structure
Sonophotocatalysis

ABSTRACT

In this communications, we report the synthesis of nickel tungstate ($NiWO_4$) nanocrystals by controlled co-precipitation at 95 °C for 2 h, followed by heat treatment at 600 °C for 2 h. The structure of the $NiWO_4$ nanocrystals was characterized using X-ray diffraction (XRD) and Rietveld refinement analysis. Field emission-scanning electron microscopy (FE-SEM) was employed to observe the shape, average size and propose a growth mechanism for the synthesized $NiWO_4$ nanocrystals. The optical behavior was investigated by ultraviolet–visible (UV–Vis) spectroscopy and first-principles quantum mechanical calculations based on the density functional theory at the B3LYP level to obtain their electronic band structure and density of states. We investigated the sonophotocatalytic (SPC) properties of $NiWO_4$ nanocrystals for degradation of remazol brilliant violet 5R (RBV5R) anionic dye using a violet light emitting diode of power 10 W. The XRD patterns indicate that the $NiWO_4$ nanocrystals heat-treated at 600 °C for 2 h have a wolframite-type monoclinic structure. The FE-SEM images showed the presence of irregular sphere-like crystals formed by self-assembly of several $NiWO_4$ nanocrystals. The experimental optical band gap energy ($E_{gap(exp)}$) was found to be 2.77 eV using UV–Vis spectroscopy and theoretical calculations indicate an indirect band gap with E_{gap} 3.91 eV, which the (O 2*p* orbitals) are predominant in the valence band and the (W 5*d* orbitals) in the conduction band and inhomogeneous electronic

* Corresponding author.
E-mail address: laeciosc@bol.com.br (L.S. Cavalcante).

https://doi.org/10.1016/j.inoche.2018.10.001
Received 10 July 2018; Received in revised form 26 September 2018; Accepted 2 October 2018
Available online 03 October 2018
1387-7003/

distribution into the lattice with the electron density map. We demonstrate for the first time that SPC activity can be enhanced after 120 min by approximately 32% for the degradation of the RBV5R anionic dye by using a $NiWO_4$ nanocatalyst.

1. Introduction

Metal tungstates exhibit the general formula AWO_4, where A is a divalent cation (A^{2+} = Mn, Fe, Co, Ni, or Cd; transition metals-*d*) network lattice. The wolframite–type metal tungstates are monoclinic with the space group (*P*2/*c*), symmetry point group (C_{2h}^4), and two molecular formula units per unit cell (Z = 2) [1,2]. The chemical coordination for the lattice former (W^{6+}) and modifier (A^{2+}) in metal tungstates are identical; the lattice former and modifier are composed of distorted octahedral [WO_6] and [AO_6] clusters, respectively [3].

In relation to the thermodynamic properties of $NiWO_4$, the literature [4–6] has shown that crystals exhibit high melting temperatures of 1400 °C [4–6]. In general, the preparation of this phase at room temperature using precursor salts and/or solvents it's not simple. By virtue of the high crystallization temperature under hydrothermal (180 °C for 12 h) [7] or ambient conditions (25 °C, 1 atm), the typical product precipitated is amorphous $NiWO_4$, which requires a thermal post-treatment ≥500 °C for 1 h [8]. Nevertheless, based on the literature, it is acknowledged that $NiWO_4$ possesses desirable physicochemical properties with possible applications in areas such as magnetism [9], photocatalytic (PC) degradation of dyes [10], supercapacitor type-hybrid electrodes [11], active electrocatalysts for hydrogen evolution reactions [12], selective detection of sub-ppm-level *p*-xylene [13], gas/humidity sensors [14], photoelectrochemical water oxidation [15], and photoluminescence (PL) [16]. In addition, other oxides may exhibit gas sensing property (ethanol gas) [17–19]. In particular, the PC properties of pure $NiWO_4$ nanocrystals at room temperature present interesting applications in environmental decontamination such as the photodegradation of methanol, 4-chlorophenol, methylene blue, methyl orange, 4-nitrophenol, rhodamine b, and alizarin red [20–24]. However, few theoretical-experimental works for $NiWO_4$ crystals have been reported in the literature so far [25,26].

Therefore, in this communications, we report on $NiWO_4$ synthesis by the controlled co-precipitation at 95 °C for 2 h followed by heat treatment at 600 °C for 2 h. The calcinated $NiWO_4$ nanocrystals were characterized by X-ray diffraction (XRD) and UV–Vis spectroscopy. The morphology and average crystal sized was observed and obtained by means of scanning electron microscopy (FE-SEM) images. In addition, we have presented the first-principles quantum mechanical calculations based on the density functional theory (DFT) to find a correlation between experimental results of the optical band gap and electronic levels. Finally, we show for the first time the enhanced sonophotocatalytic (SPC) properties of the $NiWO_4$ nanocrystals that were employed for the degradation of remazol brilliant violet 5R (RBV5R) anionic dye illuminated using a violet light-emitting diode (LED) with 10 W of power.

2. Experimental details

The synthesis of $NiWO_4$ nanocrystals is described as follows: 2.5×10^{-3} mol of sodium tungstate (VI) dihydrate ($Na_2WO_4{\cdot}2H_2O$; 99.0% purity, Sigma-Aldrich) and 2.5×10^{-3} mol of nickel (II) nitrate hydrate [$Ni(NO_3)_2{\cdot}6H_2O$; 99.999% purity, Sigma-Aldrich] were separately placed in two plastic tubes (Falcon, capacity of 50 mL) and dissolved in 50 mL of deionized water (DI-H_2O). A 50 mL solution containing the $Ni_{(aq)}^{2+}$ and $NO_{3(aq)}^{-}$ ions was prepared by dissolving Ni$(NO_3)_2{\cdot}6H_2O$ in DI-H_2O. Another 50 mL solution containing $Na_{(aq)}^{+}$ and $WO_{4(aq)}^{2-}$ ions was prepared in an volumetric flask by dissolving $Na_2WO_4.2H_2O$ in DI-H_2O, which was transferred to a 250 mL beaker (see *Supplementary data* for more details about synthesis, characterization, and SPC measurements). The theoretical calculation of the total-energy to study the optical properties of $NiWO_4$ structure was performed with the CRYSTAL14 software package [27] and in a similar way the literature has employed the DFT calculations to understand optical properties of others oxides [28] (see *Supplementary data* for more details about theoretical calculations and Brillouin zone in Fig. SD1).

3. Results and discussion

XRD patterns of the $NiWO_4$ nanocrystals synthesized by controlled co-precipitation and heat treated at 600 °C for 2 h are given in Fig. 1(a), and the corresponding FE-SEM images at different magnifications are given in Fig. 1(b–d).

The degree of structural order/disorder or periodicity of a crystalline lattice in oxide materials can be analyzed using XRD [29]. As shown in Fig. 1(a), the calcined $NiWO_4$ nanocrystals exhibits XRD patterns ascribed to the wolframite-type monoclinic structure, as determined by the Inorganic Crystal Structure Database (ICSD) card No. 15852 [30]. In order to confirm this monoclinic structure, we performed Rietveld structural refinement [31], which is based on the construction of diffraction patterns from a structural model [32]. The XRD Rietveld refinement plot is given in *Supplementary data* (Fig. SD2). The results of Rietveld refinement of the $NiWO_4$ crystals heat-treated at 600 °C for 2 h are shown in Supplementary data in Fig. SD2 and Table SD1. Moreover, the lattice parameters and atomic positions obtained from Rietveld refinement analysis (experimental data) were employed to starting the optimization of the calculated structure (theoretical model) and their optimized parameters are listed in Table SD2.

FE-SEM was used to monitor the nanocrystal shape evolution and growth process. As shown in the FE-SEM image at low magnification (10,000×) in Fig. 1(b), the $NiWO_4$ crystals presents the shape of irregular spheres with an average size of 34.5 nm. We also observe larger sphere-like $NiWO_4$ crystals with an average size of 307.2 nm (*Supplementary data* Figs. SD3(a, b)). Upon inspection of the FE-SEM image at higher magnification (80,000×) shown in Fig. 1(d), it is evident that the sphere-like $NiWO_4$ crystals grew as a result of the self-assembly of smaller $NiWO_4$ nanocrystals during both controlled co-precipitation and thermal treatment at 600 °C for 2 h.

Fig. 2(a–i) shows a schematic representation of the proposed self-assembly mechanism of the formation and growth of the $NiWO_4$ nanocrystals.

In the initial stage, both aqueous solutions are maintained at 95 °C for 15 min. The $Na_2WO_4{\cdot}2H_2O$ solution dissociated and the water (H_2O) molecules rapidly solvated the Na^+ ions and freed the WO_4^{2-} complex ions. In the second solution, the Ni^{2+} ions (d^8) are separated from the NO_3^- ions to be coordinated by six H_2O molecules, which act as weak field binders and form $[Ni(H_2O)_6]^{2+}$ positive ion complexes [33] that can then bind with the WO_4^{2-} negative complex counter ions via Coulomb interactions (Fig. 2(a–c)), promoting the nucleation of $NiWO_{4(amorphous)}$ seeds (Fig. 2(d)) [34]. These stable nuclei form and accumulate [35] when super-saturation is sufficiently high to overcome the nucleation energy barrier, and ultimately develop into crystal precipitates. At elevated temperature (600 °C for 2 h), the coalescence of several $NiWO_{4(crystalline)}$ nanocrystals occurs leading to the posterior stage, as is shown in Fig. 2(e, f), which then self-assemble to form large irregular sphere-like $NiWO_4$ crystals (Fig. 2(g, h)). The process is a random and spontaneous aggregation of $NiWO_4$ nanocrystals to form larger sphere-like $NiWO_4$ crystals and its thermodynamically driven because larger crystals are more energetically favored than smaller

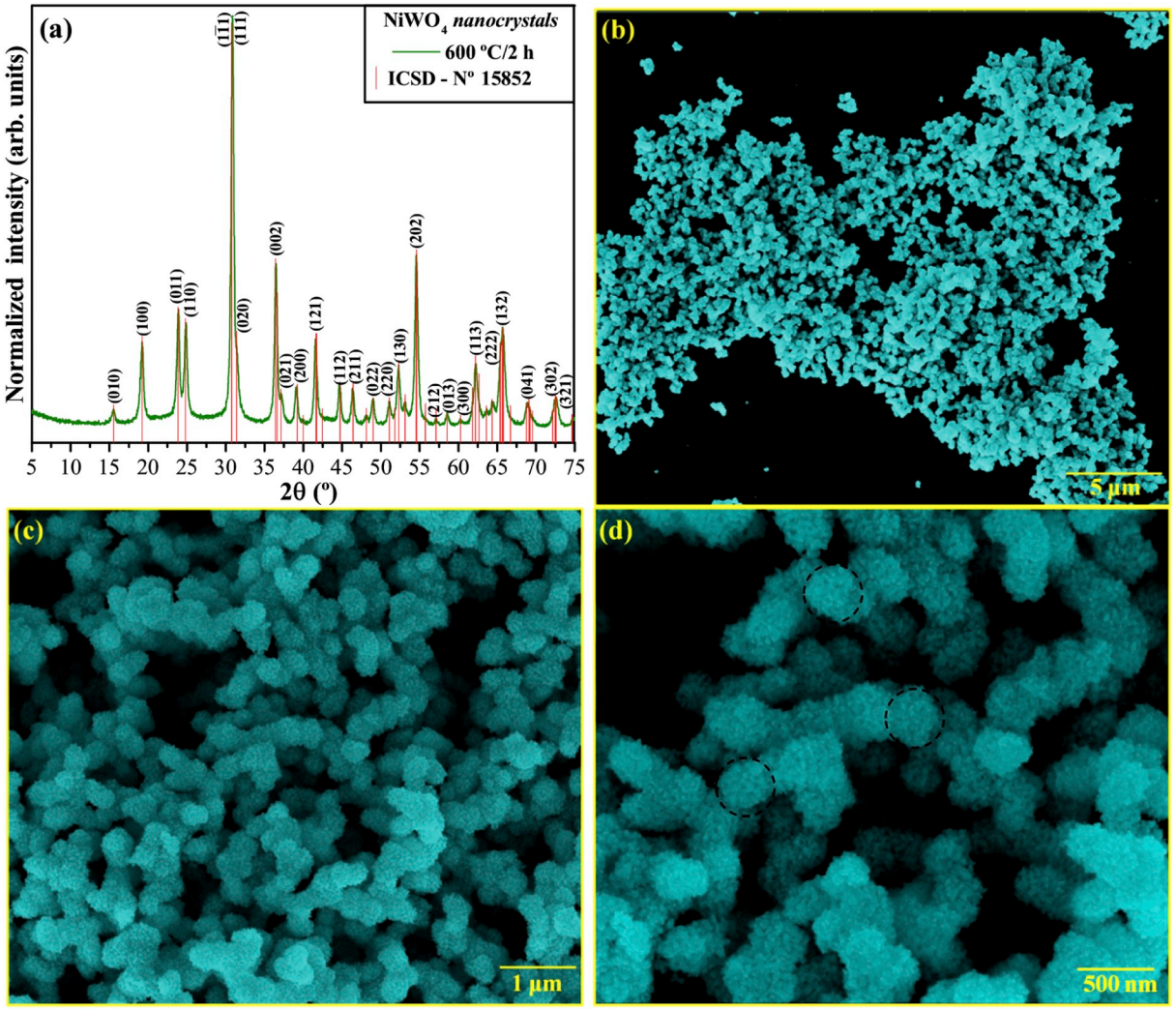

Fig. 1. (a) XRD patterns of $NiWO_4$ nanocrystals synthesized by the controlled co-precipitation method at 95 °C for 2 h and heat-treated at 600 °C for 2 h. The vertical lines in red color indicate the position and relative intensity of XRD patterns for $NiWO_4$ phase reported in ICSD file no. 15852. FE-SEM images of several $NiWO_4$ nanocrystals at (b) low magnification, (c) medium magnification, and (d) high magnification, respectively. (For interpretation of the references to color in this figure legend, the reader is referred to the web version of this article.)

crystals. Hence, we conclude that the morphology of the synthesized $NiWO_4$ is similar between the experimentally observed crystals (from FE-SEM images of Figs. 1(c, d)) and 2(i)). The possible growth mechanism of the sphere-like self-assembled $NiWO_4$ nanocrystals is illustrated in Fig. 2(a–i).

The optical band gap energy (E_{gap}) of the $NiWO_4$ nanocrystals was estimated by a modified Kubelka-Munk Eq. (1) [36]:

$$[F(R_\infty)h\nu] = C_1(h\nu - E_{gap})^n \quad (1)$$

where, $F(R_\infty)$ is the Kubelka-Munk function, R_∞ is the reflectance ($R_\infty = R_{sample}/R_{standard}$; $R_{standard}$ refers to magnesium oxide [MgO]), $h\nu$ is the photon energy, C_1 is a proportionality constant, E_{gap} is the optical band gap, and n is a constant associated with different types of electronic transitions ($n = 0.5$ for directly allowed, $n = 2$ for indirectly allowed, $n = 1.5$ for directly forbidden, and $n = 3$ for indirectly forbidden) [37]. For $NiWO_4$ nanocrystals, our theoretical calculations indicate an optical diffuse reflectance spectrum governed by indirect electronic transitions. In this phenomenon, after the electronic absorption process, electrons located in minimum energy states in the conduction band (CB) are able to relax to the maximum energy states of the valence band (VB) between different k-points in the Brillouin zone [38]. Based on this information, E_{gap} values of the $NiWO_4$ nanocrystals were calculated using $n = 2$ in Eq. (1). We plotted values of $[F(R_\infty)h\nu]^{0.5}$ against $h\nu$, and, using Eq. (1), $E_{gap(exp)}$ values were estimated by extrapolating the linear portion of UV–Vis curve to the y-axis intercept.

In Fig. 3(a), we show the UV–Vis diffuse reflectance spectrum of $NiWO_4$ nanocrystals it the optical band gap (E_{gap}) value indicated, and Fig. 3(b, c) illustrate the optimized electronic band structure (EBS) of $NiWO_4$ crystals and density of states (DOS) projected over all atoms involved in the electronic structure $NiWO_4$ crystals, Fig. 3(d) shows the electron density model in the (3) $(\bar{3}42)$ plane modeled from Rietveld refinement data and Fig. 3(e) displays the electronic density map on the (342) plane modeled from to DFT calculations, respectively.

As observed in Fig. 3(a), the profiles of the UV–Vis spectrum of the $NiWO_4$ nanocrystals indicate an optical behavior typical of structurally ordered crystalline materials in that an indirect optical band gap ($E_{gap(exp)} = 2.77$ eV) is observed. According to data experimental reported in the literature [39–41], $NiWO_4$ crystals present different optical band gap values ranging from 2.95 eV to 3.20 eV, which are all ascribed to a direct optical band gap. Therefore, our results do not agree with most of the experimental band gap values reported in the literature [39–41], since all explain that $NiWO_4$ crystals have direct

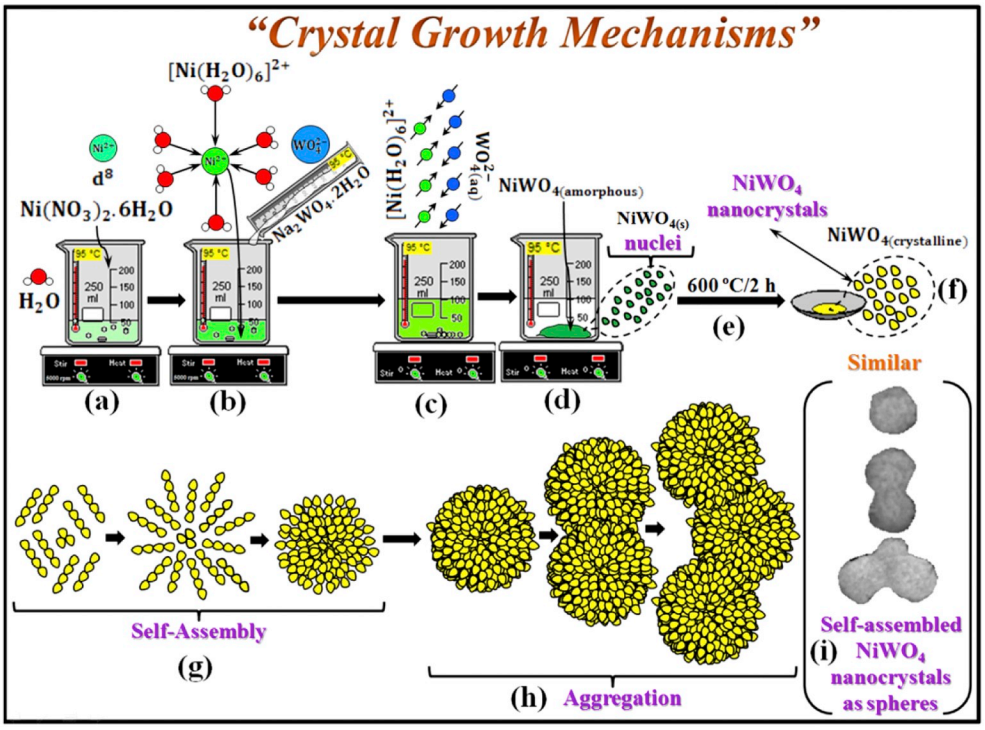

Fig. 2. Schematic representation of the synthesis of $NiWO_4$ crystals obtained by the controlled co-precipitation method at 95 °C for 2 h and heat-treated at 600 °C for 2 h: (a–c) reaction between complex ions, (d) the appearance of $NiWO_{4(amorphous)}$ and first $NiWO_{4(s)}$ nuclei, (e) conventional oven heat treatment, (f) Formation process of $NiWO_{4(crystalline)}$ nanocrystals, (g) self-assemble process of $NiWO_4$ nanocrystals, (h) aggregation of several sphere-like $NiWO_4$ crystals and (i) final of crystal growth process and similarities of sphere-like $NiWO_4$ nanocrystals.

electronic transitions between VB and CB. A small shoulder between 2.5 and 2.9 eV is observed, which is possibly due to the presence of mid-gap states (Fig. 3(a)). In transition-metal tungstates MWO_4 (M = Co, Ni, Cu, Fe), the 2*p* orbitals (O atoms) are predominantly in the VB maximum, while the CB minimum is predominantly composed of the 3*d* orbitals (Ni atoms) and 5*d* orbitals (W atoms) [42]. The analysis of the band structure, it was noticed that the $NiWO_4$ crystal is characterized by indirect electronic transitions between the different (A↔Γ) *k*-points of the VB and CB in the Brillouin zone, respectively, as shown in Fig. 3(b). This value is higher ($E_{gap(theo)}$ = 3.91 eV) that experimental value because in the theoretical calculations the system is in the ideal structure without local defects such as distortions in the octahedral $[NiO_6]$/$[WO_6]$ clusters. Additionally, these local defects resulted in the reduction of the band gap value due to the transformation of the energy levels between the VB and CB. The study of the energy levels can be better evaluated by the analysis of the density of states (DOS) as shown in Fig. 3(c). From the analysis of the DOS, it is possible to known which orbitals are involved in each band, VB and CB, in the electronic transitions. The Fig. 3(c) shows that the projected DOS on the O atoms is principally determined in the VB with the 2*p* orbitals and a minor contribution from 3*d* orbitals from Ni atoms while the CB is mainly determined by the 5*d* orbitals from W atoms with minor contributions of 2*p* and 3*d* orbitals from O and Ni, respectively. Focusing on the electronic density near the band edges, the VB is predominantly composed of the O $2p_x$ and $2p_y$ orbitals, whereas the bottom of the $NiWO_4$ crystal is formed by $3d_z^2$ and $3d_{xz}$ orbitals from Ni atoms and $5d_z^2$, $5d_{xz}$ and $5d_{x-y}^{2\ 2}$ orbitals from W atoms. Finally, in Fig. 3(d) we have the electron density model calculated using the Fourier transform for structure factors from the structure parameters and atomic scattering factors of free atoms obtained from the Rietveld refinement for the $NiWO_4$ crystal. The data were used in the VESTA software version 3.4.4 [43] to model the electron density map. These figures display color scales for each plane, which indicates zones with high and low electronic densities. The blue regions are related to the absence of electronic charge, while the red areas exhibit a high electronic density in the $(\bar{3}42)$ plane with distance from origin of 1.48 Å. Moreover, it is possible to verify the presence of distributions non-homogeneous near the Ni−O bonds related to an atomic displacement, suggesting the existence of large distortions between Ni and O atoms or distortions in the octahedral $[NiO_6]$ clusters and Fig. 3(e) depicts the electronic density map in the (342) plane which have the isolines on the atoms represent the charge density and this map then represents the difference of charges between atoms. Therefore, our experimental and theoretical results are in good agreement.

Fig. 4(a) illustrates the photolysis of the RBV5R dye solution, in Fig. 4(b) is display the SPC degradation of the RBV5R dye solutions with $NiWO_4$ acting as a catalyst, which was monitored by the temporal changes in the UV–Vis absorbance of the dye. The degradation curves (C_n/C_0 vs. time) of the RBV5R dye aqueous solutions both with and without the $NiWO_4$ nanocatalyst are shown in Fig. 4(c); the rate constants (k) obtained from the curves are shown in Fig. 4(d).

As shown in Fig. 4(a) the UV–Vis spectral intensity of the RBV5R dye solution does not significantly change upon 120 min of photolysis exposure, and its within 2% in the case of maximum absorption, indicating a large resistance of the RBV5R dye to violet-LED illumination. Conversely, a significant reduction in UV–Vis absorption is observed after 120 min of exposure to violet-LED assisted ultrasound, or sonophotocatalysis, indicating a significant reduction in RBV5R concentration. In traditional photocatalysis, the active sites on the catalyst oxide would be reduced due to the aggregation of catalyst particles. On the other hand, in sonophotocatalysis ultrasound waves promote absorption-desorption events that significantly decrease the aggregation of catalyst nanocrystals in the RBV5R dye solution, leading to a better catalytic performance of the $NiWO_4$ crystals in solution [42]. As shown in Fig. 4(b), about 32% reduction in the maximum absorption (λ_{max} = 560 nm) of the RBV5R dye aqueous solution has been noticed up until 120 min of photolysis, which demonstrates the utility of both the $NiWO_4$ nanocrystals as well as the SPC process for enhanced catalysis and degradation. A synergistic effect of ultrasound and UV light irradiation is observed, which enabled the formation of more hydroxyl radicals (HO^*) in the VB and superoxide radical anions ($O_2^{\cdot}$) in the CB that are highly oxidizing and necessary for the degradation process.

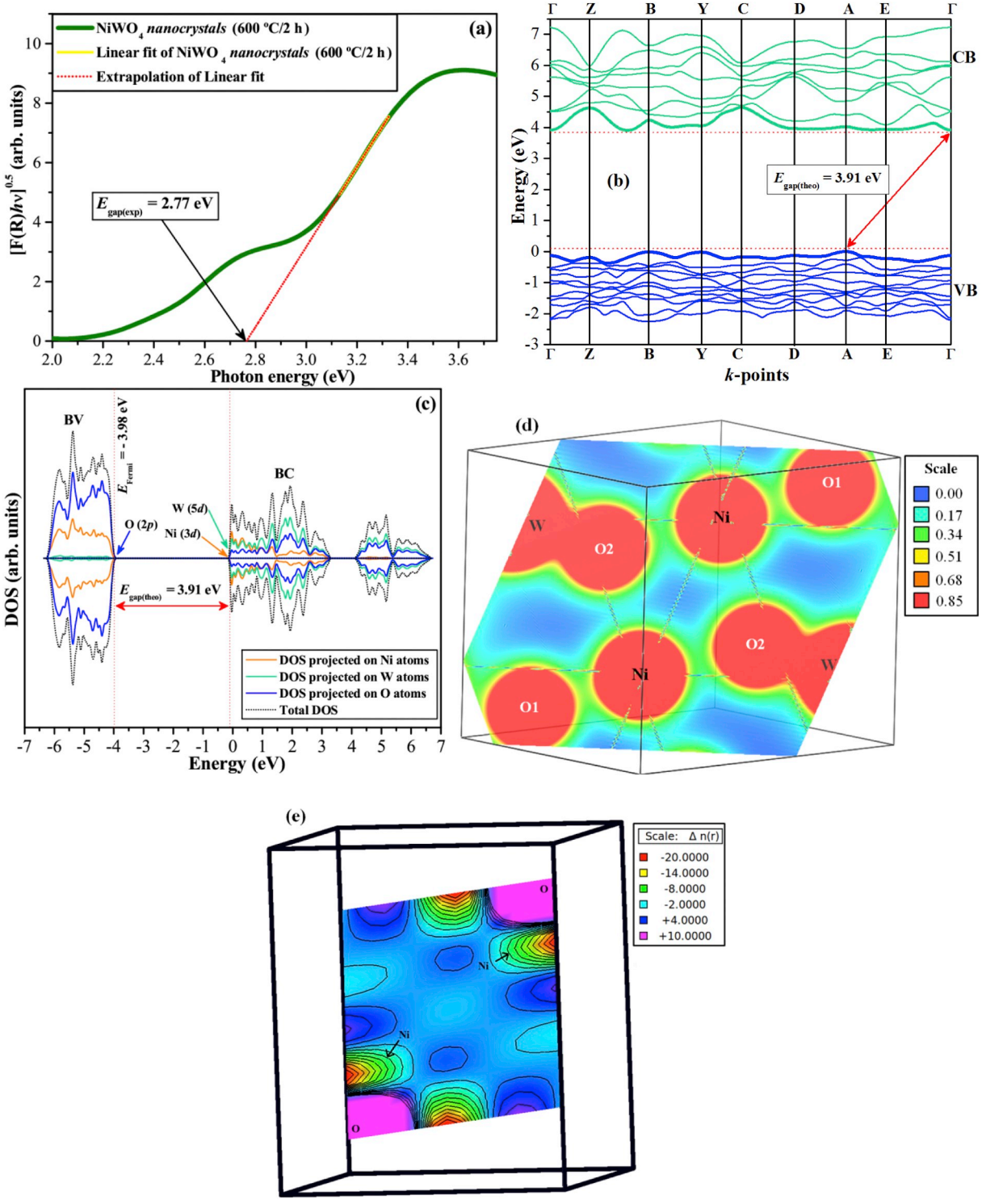

Fig. 3. (a) UV–Vis spectrum of $NiWO_4$ nanocrystals synthesized by the controlled co-precipitation method at 95 °C for 2 h and heat-treated at 600 °C for 2 h, (b) optimized EBS, (c) total DOS projected on the atoms of $NiWO_4$ crystals in the antiferromagnetic spin configuration, (d) electron density maps in the ($\bar{3}42$) plane, and on the (e) (342) plane respectively.

To quantitatively understand the RBV5R dye degradation reaction kinetics using the $NiWO_4$ nanocatalyst (Fig. 4(c)), we applied the pseudo-first-order model expressed in Eq. (2) to obtain the rate constants (k):

$$-\ln\left(\frac{C_n}{C_0}\right) = kt \tag{2}$$

where, C_0 is the initial concentration (t = 0 min) of the aqueous dye solution, C_n is the concentration of the aqueous dye solution at different times (n = 10 min, 20 min, etc.) of illumination with violet-LED, t is the time, and k is the pseudo-first order rate constant. Eq. (2) has generally been used for photocatalytic degradation processes if the initial pollutant concentration is low (1×10^{-5} mol/L). According to eq. (2), a plot of $[-\ln(C_n/C_0)]$ as a function of t gives a straight line with slope k. As shown in Fig. 4(d), the rate constant without the catalyst for the degradation of RBV5R dye is quite small ($k_{wc\text{-}RBBR}$

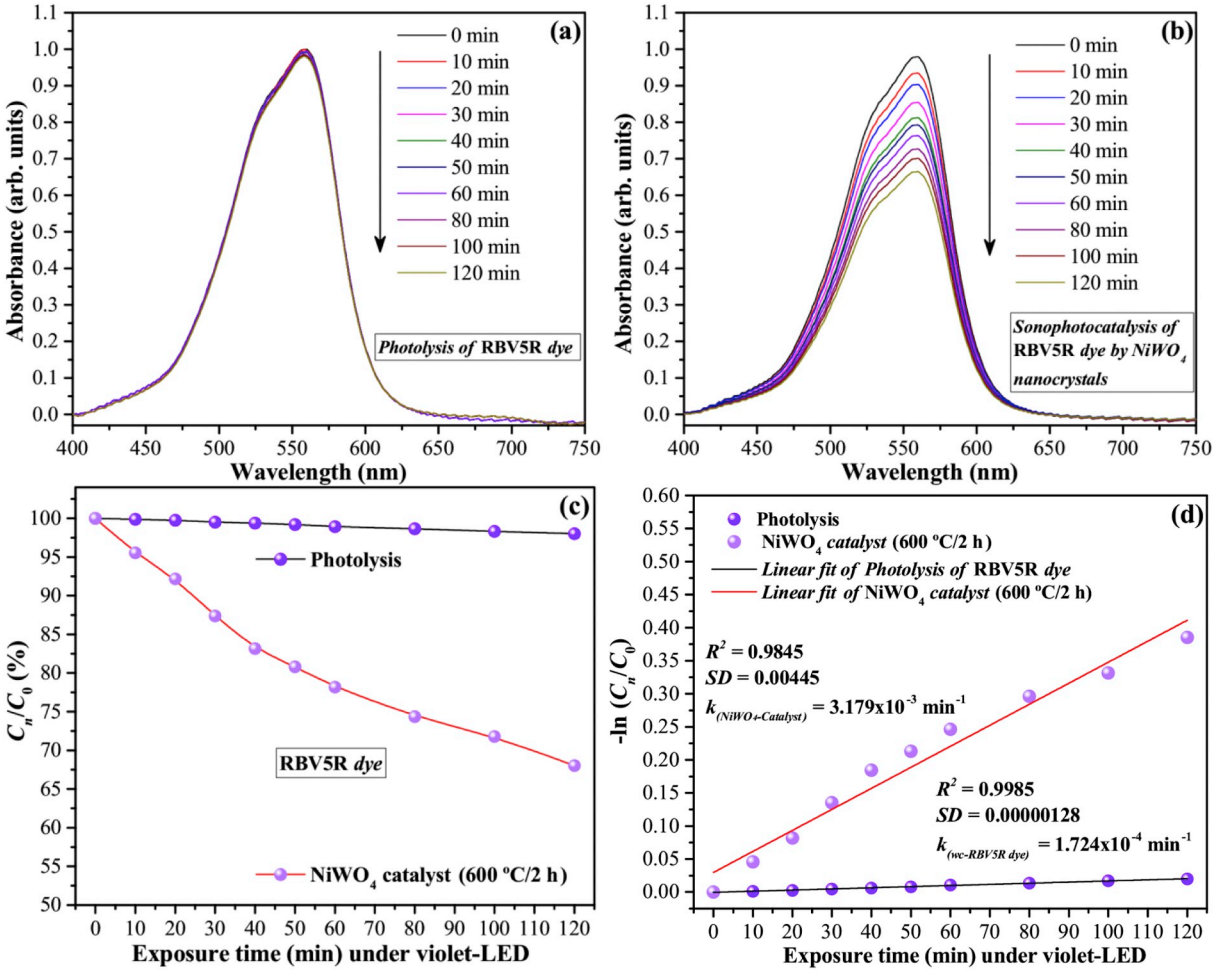

Fig. 4. (a) Evolution of UV–vis absorption spectra after 120 min of violet-LED illumination for photolysis of RBBR dyes, (b) evolution of UV–vis absorption spectra up-to 120 min of violet-LED illumination for the sonophotodegradation of RBBR dye by the $NiWO_4$ catalysts nanocrystals, (c) kinetic of weight-based photolysis of RBBR dye and sonophotocatalytic degradation of RBBR dye by the $NiWO_4$ nanocatalysts and (d) first-order kinetic without and with $NiWO_4$ nanocatalysts, respectively. (For interpretation of the references to color in this figure legend, the reader is referred to the web version of this article.)

$_{dye} = 1.724 \times 10^{-4}\,min^{-1}$), indicating minimal degradation upto 120 min of violet–LED exposure. On the other hand, as displayed in Fig. 4(d), the rate constant when including the catalytic $NiWO_4$ nanocrystals is ≈18.5 times higher ($k_{NiWO4\text{-}Catalyst)} = 3.179 \times 10^{-3}\,min^{-1}$), demonstrating the enhanced degradation efficiency of $NiWO_4$ and the SPC process. The obtained results for the correlation coefficient and standard deviation showed good statistical values for our $NiWO_4$ nanocrystals.

4. Conclusions

In summary, sphere-like self-assembled $NiWO_4$ nanocrystals were successfully synthesized via controlled co-precipitation at 95 °C for 2 h, followed by heat-treatment at 600 °C for 2 h. The XRD patterns and Rietveld refinement data confirm that the $NiWO_4$ nanocrystals have a long-range order with wolframite-type monoclinic structure. FE-SEM images showed the presence of $NiWO_4$ nanocrystals with an average particle size of 34.5 nm. A proposed nucleation and growth process of the self-assembled $NiWO_4$ nanocrystals was discussed. The optical band gap of $NiWO_4$ nanocrystals was found to be $E_{gap(exp)}$ = 2.77 eV with the possible existence of intermediary energy states within the band gap. The theoretical calculation indicated that the EBS of $NiWO_4$ crystals in the antiferromagnetic spin configuration are characterized by indirect electronic transitions. According to the DOS analyses, the energy states in the VB is constituted mainly from (O 2*p*) orbitals, while in the CB has a major contribution related to (W 5*d*) orbitals. Our electron density maps showed an inhomogeneous distribution of charges between distorted octahedral [NiO_6] clusters. We demonstrated a SPC process that exhibits higher degradation efficiency compared to simple photolysis due to the synergistic effect of ultrasound and violet-LED irradiation, which promotes the formation of active oxidizing species that are necessary for the degradation of the RBV5R dye.

Acknowledgements

The Brazilian authors acknowledge the financial support of the Brazilian research financing institutions: CNPq (350711/2012-7; 479644/2012-8; 312318/2017-0; 150949/2018-9), FAPESP (13/07296-2) and CAPES.

Appendix A. Supplementary data

Supplementary data to this article can be found online at https://doi.org/10.1016/j.inoche.2018.10.001.

References

[1] S.M.M. Zawawi, R. Yahya, A. Hassan, H.N.M.E. Mahmud, M.N. Daud, Chem. Cent. J. 7 (2013) 80–89.
[2] P. Parhi, T.N. Karthik, V. Manivannan, J. Alloys Compd. 465 (2008) 380–386.
[3] M.A.P. Almeida, L.S. Cavalcante, M. Siu Li, J.A. Varela, E. Longo, J. Inorg.

Organomet. Polym. 22 (2012) 264–271.
[4] R.O. Keeking Jr., The structure of $NiWO_4$, Acta Cryst 10 (1957) 209–2013.
[5] C.P. Landee, E.F. Westrum Jr., J. Chem. Thermodyn. 8 (1976) 471–491.
[6] S. Oishi, Y. Furuichi, K. Kitajima, J. Mater. Sci. 31 (1996) 5309–5312.
[7] R. Kumar, T. Bhuvana, A. Sharma, RSC Adv. 7 (2017) 42146–42158.
[8] H.Y. He, L.Y. Cao, Z. He, J. Lu, Int. J. Nano Biomater. 5 (2014) 113–124.
[9] C.B. Liu, Z.Z. He, Y.J. Liu, R. Chen, M.M. Shi, H.P. Zhu, C. Dong, J.F. Wang, J. Magn. Magn. Mater. 44 (2017) 190–192.
[10] N. Helaïli, A. Boudjamaa, M. Kebir, K. Bachari, Environ. Sci. Pollut. Res. 24 (2017) 6481–6491.
[11] S. Chen, G. Yang, Y. Jia, H. Zheng, J. Mater. Chem. A 5 (2017) 1028–1034.
[12] S.F. Anis, B.S. Lalia, A.O. Mostafa, R. Hashaikeh, J. Mater. Sci. 52 (2017) 7269–7281.
[13] T.H. Kim, C.H. Kwak, J.H. Lee, ACS Appl. Mater. Interfaces 9 (2017) 32034–32043.
[14] T. Zhong, X. Liang, H. Zhang, S. Yang, J. Li, B. Baofu, G. Lu, Sens. Lett. 9 (2011) 307–310.
[15] M.I. Ahmed, A. Adam, A. Khan, M.N. Siddiqui, Z.H. Yamani, M. Qamar, Mater. Lett. 177 (2016) 135–138.
[16] H.Y. He, Mater. Res. Innov. 12 (2008) 138–141.
[17] L. Zhu, W. Zeng, Y. Li, Mater. Lett. 228 (2018) 331–333.
[18] L. Zhu, Y. Li, W. Zeng, Appl. Surf. Sci. 427 (2018) 281–287.
[19] L. Zhu, W. Zeng, J. Yang, Y. Li, Mater. Lett. 230 (2018) 297–299.
[20] U.M. García-Pérez, A. Martínez-De La Cruz, J. Peral, Electrochim. Acta 81 (2012) 227–232.
[21] T. Montini, V. Gombac, A. Hameed, L. Felisari, G. Adami, P. Fornasiero, Chem. Phys. Lett. 498 (2010) 113–119.
[22] M.M.J. Sadiq, U.S. Shenoy, D.K. Bhat, J. Phys. Chem. Solids 109 (2017) 124–133.
[23] M. Hao, X. Meng, Y. Miao, Solid State Sci. 72 (2017) 103–108.
[24] K. Santhi, C. Rani, S. Karuppuchamy, J. Mater. Sci. Mater. Electron. 27 (2016) 5033–5038.
[25] N. Doudin, S. Pomp, M. Blatni, R. Resel, M. Vorokhta, J. Goniakowski, C. Noguera, F.P. Netzer, S. Surnev, Surf. Sci. 659 (2017) 20–30.
[26] A. Kuzmin, A. Kalinko, R.A. Evarestov, Cent. Eur. J. Phys. 9 (2011) 502–509.
[27] R. Dovesi, R. Orlando, A. Erba, C.M. Zicovich-Wilson, B. Civalleri, S. Casassa, L. Maschio, M. Ferrabone, M. De La Pierre, P. D'Arco, Y. Noel, M. Causa, M. Rerat, B. Kirtman, Int. J. Quantum Chem. 114 (2014) 1287–1317.
[28] K.M. Wong, S.M. Alay-E-Abbas, Y. Fang, A. Shaukat, Y. Lei, J. Appl. Phys. 114 (2013) 034901-1–034901-10.
[29] V.H. Weitzel, Z. Kristallogr. 144 (1976) 238–258.
[30] H.M. Rietveld, J. Appl. Crystallogr. 2 (1969) 65–71.
[31] H.M. Rietveld, Line profiles of neutron powder-diffraction peaks for structure refinement, Acta Crystallogr. 22 (1967) 151–152.
[32] Y.Y. Wei, X. Lai, J. Bi, B. Li, D.J. Gao, J. Funct. Mater. 41 (2010) 1532–1535.
[33] M.R.D. Bomio, L.S. Cavalcante, M.A.P. Almeida, R.L. Tranquilin, N.C. Batista, P.S. Pizani, M. Siu Li, J. Andres, E. Longo, Polyhedron 50 (2013) 532–545.
[34] J. Park, J. Joo, S.G. Kwon, Y. Jang, T. Hyeon, Angew. Chem. Int. Ed. 46 (2007) 4630–4660.
[35] P. Kubelka, F. Munk, Z. Tech. Phys. 12 (1931) 593–601.
[36] A.E. Morales, E.S. Mora, U. Pal, Rev. Mex. Fis. Suppl. 53 (2007) 18–22.
[37] K. Hoang, M. Oh, Y. Cho, RSC Adv. 8 (2018) 4191–4196.
[38] M. Masteri-Farahani, M. Saemi, J. Mater. Sci. Mater. Electron. 28 (2017) 1328–1335.
[39] S.M. Alshehri, J. Ahmed, A.M. Alzahrani, T. Ahamad, New J. Chem. 41 (2017) 8178–8186.
[40] S.M. El-Sheikh, M.M. Rashad, J. Clust. Sci. 26 (2015) 743–757.
[41] S. Shepard, M. Smeu, Comput. Mater. Sci. 143 (2018) 301–307.
[42] F.F. Harno, A. Taufik, R. Saleh, AIP Conf. Proc. 1862 (2017) 030021–030025.
[43] K. Momma, F. Izumi, J. Appl. Crystallogr. 44 (2011) 1272–1276.